

# TetraDiffusion: Tetrahedral Diffusion Models for 3D Shape Generation

Nikolai Kalischek\*    Torben Peters\*    Jan D. Wegner    Konrad Schindler  
Photogrammetry and Remote Sensing, ETH Zürich  
{nkalischek, tpeters, jwegner, schindler}@ethz.ch

<https://tetradiffusion.github.io>



Figure 1. *TetraDiffusion* is a 3D denoising diffusion model that operates on a tetrahedral grid to enable the generation of high-resolution 3D shapes in seconds. All depicted meshes are shown without any postprocessing, hole-filling or smoothing.

## Abstract

*Probabilistic denoising diffusion models (DDMs) have set a new standard for 2D image generation. Extending DDMs for 3D content creation is an active field of research. Here, we propose TetraDiffusion, a diffusion model that operates on a tetrahedral partitioning of 3D space to enable efficient, high-resolution 3D shape generation. Our model introduces operators for convolution and transpose convolution that act directly on the tetrahedral partition, and seamlessly includes additional attributes such as color. Remarkably, TetraDiffusion enables rapid sampling of detailed 3D objects in nearly real-time with unprecedented resolution. It's also adaptable for generating 3D shapes conditioned on 2D images. Compared to existing 3D mesh diffusion techniques, our method is up to 200 times faster in inference speed, works on standard consumer hardware, and delivers superior results.*

## 1. Introduction

The growing demand for virtual content has sparked a wave of research to automate the laborious and costly generation of 3D assets. At the heart of this endeavor lies the

search for powerful and flexible 3D representations to encode, store and manipulate the geometry and topology of 3-dimensional objects. In this work, we describe a novel, highly efficient generative model that is able to produce high-quality surface meshes in seconds.

Following the rise of probabilistic denoising diffusion models (DDMs) for image generation [9, 19, 36, 37, 43], there have been several attempts to extend their generative capabilities to 3D [15, 26, 28, 53, 54]. It is relatively straightforward to transfer the DDM principle – gradual per-point perturbations with Gaussian noise – to voxels or points in 3D space, and this has already led to interesting results [28, 53, 54]. However, these representations also come with their own disadvantages. Voxels are a natural extension of 2D pixels and amenable to well-established neural architectures based on discrete 3D convolutional operators, yet they are notoriously memory-hungry and therefore limited in terms of resolution. Point clouds, on the other hand, are sampled irregularly and avoid unnecessary discretization of empty space, but they lack connectivity information and have no direct notion of the underlying surfaces. Both representations face additional challenges when converting them to a surface mesh, as one must trade off smoothing and loss of detail against surface noise and topological artifacts. An alternative could be to directly work

\* Equal contributions.

with meshes, but handling explicit meshes is cumbersome and restricted by the fixed surface topology.

Instead, we turn to a hybrid representation that combines the advantages of both worlds, namely a tetrahedral decomposition of 3D space. We develop neural operators that directly act on the tetrahedral representation, and thus allow for fast and memory-efficient learning. This is in contrast to methods that embed the tetrahedral representation in a voxel grid of much higher resolution, thus inheriting the limitations of voxel models [26]. Tetrahedral decompositions of 3D space have their origin in engineering and physics simulation and have also been used for volumetric modelling in graphics [21, 32], but they have only recently been adopted in the context of deep learning [12, 14, 41]. By combining the flexibility and structure of the tetrahedral grid with the generative power of DDMs, our model overcomes some of the limitations of existing 3D diffusion frameworks. A key ingredient of our method is a carefully predefined neighborhood topology of the space-filling tetrahedral decomposition [12] that enables well-defined convolutional operators and makes it easy to extract a surface mesh with the help of a differentiable Marching Tetrahedra scheme [14].

In the spirit of KPConv [45] and graph convolutions [3, 23, 48], we equip that representation with convolution (and transposed convolution) kernels that operate directly on the deformable tetrahedral structure. These operations make it possible to construct a U-Net architecture [38] in the tetrahedralized space, which, in turn, is the computational core of a denoising diffusion model. Our DDM learns to transform random noise into a 3D object shape by predicting both a per-vertex signed distance field and an individual per-vertex displacement, depicted in Fig. 2.

Our formulation has several benefits. Like in a point cloud, the vertices of the tetrahedral grid can be moved around to align with a desired surface. But at the same time they retain a uniquely defined neighborhood connectivity, which ensures that one can readily extract a topologically sound surface mesh, and obviates the need to train an additional surface reconstruction network [33]. Moreover, our network can be deployed on a multi-resolution hierarchy of tetrahedral decompositions, which makes both training and inference memory-efficient and computationally affordable. Empowered by the modest computational cost we are able to run diffusion at a higher native resolution (in our experiments  $>5$  million tetrahedra, see Sec. 3) and to reconstruct 3D shapes with unprecedented detail. To further reduce training time, our proposed tetrahedral convolution layers make it possible to exploit sparsity by pruning tetrahedra in unoccupied regions of 3D space. Going beyond purely geometric object properties (captured by signed distance values and vertex offsets), we extend the tetrahedral representation and the associated Marching Tetrahedra scheme [41] to unrestricted feature vectors, such that it becomes possible

to diffuse and extract further attributes like color. The extended Marching Tetrahedra algorithm remains fully differentiable. Consequently one can guide the diffusion during inference, *e.g.* towards smoother shapes, larger or smaller volume, or specific colors. Moreover one can drive the sampled shapes to resemble existing examples, renderings or textual descriptions, similar to classifier-free guidance [18] and regularization [37]. In summary, our key contributions are:

1. To the best of our knowledge, we propose the first 3D denoising diffusion model that operates entirely on a tetrahedral representation.
2. We design convolution operators and up- and downsampling kernels on the tetrahedral grid.
3. We show that *TetraDiffusion* enables efficient training and near real-time inference at unprecedented resolution, on consumer hardware.
4. We extend our tetrahedral DDM to include color, and to allow for 3D shape generation guided by images scraped from the internet.

## 2. Related work

**3D Generative Models.** Compared to their 2D counterparts, 3D generative models have to choose among a wider range of data representations. Most dominant are voxels and point clouds, for which it is straightforward to adapt the 2D formulations [1, 51, 52]. Early work directly treats point clouds as matrices to make them amenable to standard neural architectures [11], or rasterizes 3D data into a voxel grid in order to apply conventional 3D convolutions [2, 50]. To overcome fixed structures and to induce permutation invariance, PointFlow [51] first samples from a shape distribution and in a second step samples from the distribution of points given the corresponding shape prior.

Another prominent stream of work relies on implicit representations. The authors of [7] introduce an implicit field decoder to learn a signed distance function. The network is trained in adversarial fashion to predict the distance from the surface when presented a point coordinate and its associated feature encoding. In [4], shapes are represented as gradient fields over the logarithmic surface density, taking advantage of score-based generative models [43]. Similarly, [1] learn a shape prior with an auto-encoder and GAN in latent space. Our model does not rely on adversarial training or latent interpolation, rather we train directly on input encodings.

A combination of explicit and implicit representations is explored in GET3D [13]. Similar to our work, 3D shapes are described via signed distances and deformation vectors on a tetrahedral grid with fixed topology. Their tetrahedral representation is encoded in separate triplane representations for geometry and texture that are trained in an adversarial manner with rendering losses, making use of the dif-

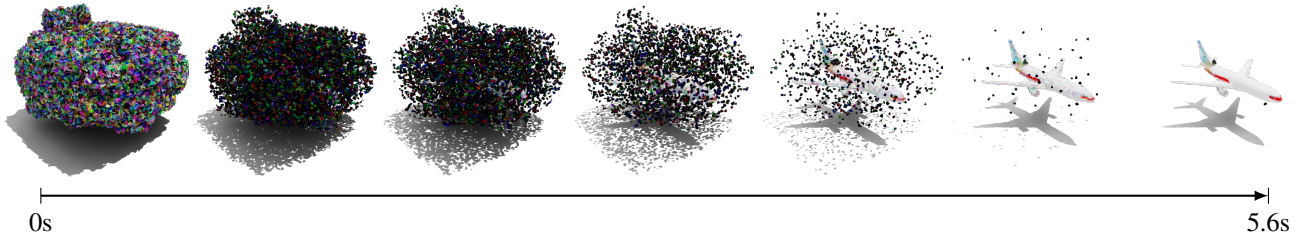


Figure 2. Exemplary reverse diffusion sequence starting from a noisy tetrahedral grid to a final textured mesh in a few seconds.

ferentiable Marching Tetrahedra [41]. Instead of projecting into triplanes, TetGAN [14] directly operates on the tetrahedralized cuboid with an auto-encoder, supervised with ground truth features as well as global and local adversarial losses. Somewhat similar to our work they define convolutions and up-/down-sampling operators on entire tetrahedra, which in their setting is straightforward as each tetrahedron has exactly four neighbours. In contrast, we extend those operations to act on vertices directly so as to allow for displacements, in the spirit of DMTet [41]. Our more general formulation naturally offers more flexibility and representation power, since every vertex can be aligned individually in contrast to the tetrahedral occupancy field in TetGAN, which only allows aligning a tetrahedron as a whole.

**3D Diffusion Models.** With the rise of DDMs, various 3D representations have been transferred to the diffusion setting [28, 29, 53, 54]. Point-voxel diffusion incorporates a point-voxel CNN [54] to directly apply diffusion on the hybrid representation. Similarly, [28] directly diffuses point clouds conditioned on a latent shape representation generated with a normalizing flow. LION [53] uses DDMs in latent space and maps the latent encoding back to a point cloud with a VAE. By itself this generates noisy point clouds, which is why they must train an additional network [33] to turn those into smooth meshes. To circumvent that extra surface extractor, 3DGen [15] introduces a two-stage training pipeline consisting of a triplane VAE and a separately trained latent diffusion model in triplane space. Somewhat similarly, [42] first train a decoder that maps triplane features to occupancy grids, then train a 2D diffusion model to generate those triplanes. In contrast, our method only requires *single-stage training* and no separate decoder, by natively operating on the tetrahedral 3D representation.

Perhaps the closest work to ours is MeshDiffusion [26], which also maps meshes to a deformable tetrahedral grid and performs diffusion on that representation. However, to circumvent the lack of convolutional operators for that grid they embed the tetrahedra in a higher-resolution regular voxel grid. This makes it possible to employ conventional 3D convolutions, but largely sacrifices the benefit of the tetrahedral representation: the voxelization is extremely

inefficient, as it leads to a cubic increase in memory footprint and computation without adding any information. By defining convolutions directly on the spatially sparse vertices of the tetrahedral grid our model avoids that large overhead and allows for a finer tetrahedralization that captures higher-resolution details.

### 3. Background

**Tetrahedral Grid.** Following [41], we represent shapes within a given cuboid  $\mathcal{T}$  with a signed distance field and a displacement field that are both defined on the vertices of the same, space-filling tetrahedral decomposition of  $\mathcal{T}$ . We refer to that structure as the *tetrahedral grid*, with vertices  $V_{\mathcal{T}} \in \mathbb{R}^{N \times 3}$  and tetrahedra  $T \in \mathbb{N}^{K \times 4}$ . A nearly regular decomposition can be found via close-packed tetrahedral tiling with the A15 lattice [10]. Tetrahedral grid resolution refers to the grid spacing used in the iso-surface stuffing algorithm. A tetrahedralized cube of resolution  $R$  contains  $0.72 \cdot R^3$  tetrahedra. Note that a given number of tetrahedra can capture more detail than the same number of voxels, as they can be deformed to better follow the surface. Each tetrahedron  $T_k$  consists of four vertices  $\{v_{k1}, v_{k2}, v_{k3}, v_{k4}\}$  and corresponding edges to form a simplex, *i.e.*, the connectivity is predefined and fixed during training and inference. Each vertex is assigned a displacement  $\Delta_v$  and a signed distance value  $s_v$ . The SDF provides an implicit surface representation, whereas the displacements serve to precisely align it with the actual object surface. Conveniently, one can extract a surface *mesh* from  $\mathcal{T}$  with Deep Marching Tetrahedra (DMTet, [41]). In Section 4, we extend the tetrahedral representation to arbitrary feature vectors, such that additional vertex attributes (*e.g.*, color) can be propagated to the final mesh.

**Diffusion.** Denoising diffusion models can be seen as restricted, hierarchical Markovian VAEs [27] that learn to approximate the data distribution  $p(\mathbf{x})$  with a sequence of steps. In the variational formulation [20, 22] the steps are indexed by a continuous time variable  $t \in [0, 1]$ . At the final time step  $T = 1$  the latent variables  $\mathbf{z}_t$  should be normally distributed,  $q(\mathbf{z}_T) = \mathcal{N}(\mathbf{z}_T; \mathbf{0}, \mathbf{I})$ . The forward process of

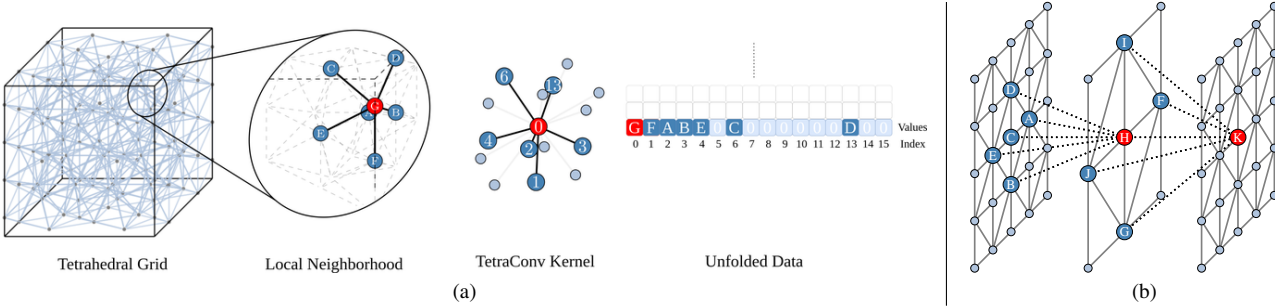


Figure 3. (a) Tetrahedral convolution for kernel size  $m = 16$ . The TetraConv kernel defines the ordering and padding for every local neighborhood. The center vertex, where the convolution aggregates, is marked in red and the neighborhood in dark blue. Missing vertices (light blue) are padded with zeros. (b) Strided convolution  $H = \text{TetraConv}(A, B, C, D, E)$  and transposed convolution  $K = \text{TetraConv}(F, G, H, I, J)$  accumulate information from the nearest neighbors in their preceding layers. Operators are depicted in 2D.

the marginals  $q(\mathbf{z}_t | \mathbf{x})$  is Gaussian and given by

$$q(\mathbf{z}_t | \mathbf{x}) = \mathcal{N}(\mathbf{z}_t; \alpha_t \mathbf{x}, \sigma_t^2 \mathbf{I}), \quad (1)$$

where  $\text{SNR}(t) = \frac{\alpha_t^2}{\sigma_t^2}$  is the signal-to-noise ratio, assumed to decrease strictly monotonically in time, and  $\alpha_t$  and  $\sigma_t^2$  are strictly positive for all  $t$ . Consequently,  $\mathbf{z}_t$  will be increasingly noisy over time. We fix  $\alpha_t^2 = 1 - \sigma_t^2$ , corresponding to a variance-preserving process [44]. Under the Markov assumption the forward transition kernels for  $t > s$  are also Gaussian and given by:

$$q(\mathbf{z}_t | \mathbf{z}_s) = \mathcal{N}(\mathbf{z}_t; \alpha_{t|s} \mathbf{z}_s, \sigma_{t|s}^2 \mathbf{I}), \quad (2)$$

where  $\alpha_{t|s} = \frac{\alpha_t}{\alpha_s}$  and  $\sigma_{t|s}^2 = \sigma_t^2 - \alpha_{t|s}^2 \sigma_s^2$ . A common noise schedule is  $\alpha_t = \cos(\pi t/2)$ , which under variance preservation leads to a signal-to-noise ratio of  $\text{SNR}(t) = \frac{1}{\tan(\pi t/2)}$ .

We are interested in learning the reverse diffusion process. While  $q(\mathbf{z}_s | \mathbf{z}_t)$  is in general intractable as it requires integration over the whole dataset, conditioning it on a data sample  $\mathbf{x}$  gives rise to a closed-form solution:

$$q(\mathbf{z}_s | \mathbf{z}_t, \mathbf{x}) = \mathcal{N}(\mathbf{z}_s; \mu_{s,t}(\mathbf{z}_t, \mathbf{x}), \sigma_{s,t}^2 \mathbf{I}), \quad (3)$$

where  $\mu_{s,t}(\mathbf{z}_t, \mathbf{x}) = \frac{\alpha_{t|s} \sigma_s^2}{\sigma_t^2} \mathbf{z}_t + \frac{\alpha_s \sigma_{t|s}^2}{\sigma_t^2} \mathbf{x}$  and  $\sigma_{s,t}^2 = \sigma_{t|s}^2 \frac{\sigma_s^2}{\sigma_t^2}$ . As  $\mathbf{x}$  is only available during training, it is replaced by a neural network prediction  $\hat{\mathbf{x}}_\theta(\mathbf{z}_t; t) \approx \mathbf{x}$ . An equivalent interpretation of the denoising model is as a score model, which in the infinite data limit covers to the marginal distribution  $q(\mathbf{z}_t)$  [43].

To train  $\hat{\mathbf{x}}_\theta(\mathbf{z}_t; t)$  one optimizes the variational lower bound of the marginal log-likelihood

$$\mathcal{L}(\mathbf{x}) = -\frac{1}{2} \mathbb{E}_{\substack{\epsilon \sim \mathcal{N}(0, \mathbf{I}) \\ t \sim \mathcal{N}(0, \mathbf{I})}} \left[ \text{SNR}'(t) \|\mathbf{x} - \hat{\mathbf{x}}_\theta(\mathbf{z}_t; t)\|_2^2 \right], \quad (4)$$

where  $\text{SNR}'(t) = d\text{SNR}/dt$  and  $\mathbf{z}_t = \alpha_t \mathbf{x} + \sigma_t \epsilon$ . Instead of parametrizing the model to directly recover  $\mathbf{x}$  from its

corrupted version  $\mathbf{z}_t$ , one can predict the noise  $\hat{\epsilon}$  and recover  $\hat{\mathbf{x}}$  from  $\hat{\mathbf{x}} = \frac{\mathbf{z}_t}{\alpha_t} - \sigma_t \frac{\hat{\epsilon}}{\alpha_t}$ . Since that objective tends to destabilize training near  $t = 1$ , we use the more robust  $v$ -parametrization [40],  $\hat{\mathbf{v}}_t = \alpha_t \hat{\epsilon}_t - \sigma_t \hat{\mathbf{x}}$ . Note that  $\hat{\mathbf{x}} = \alpha_t \mathbf{z}_t - \sigma_t \hat{\mathbf{v}}_t$ . Once trained, we can sample from our data distribution with ancestral sampling. Setting  $\epsilon \sim \mathcal{N}(0, \mathbf{I})$ , we starting at  $\mathbf{z}_1 \sim \mathcal{N}(0, \mathbf{I})$  and iteratively denoise it according to

$$\mathbf{z}_s = \frac{\alpha_t \sigma_s^2}{\alpha_s \sigma_t^2} \mathbf{z}_t + \frac{\alpha_s \sigma_{t|s}^2}{\sigma_t^2} \hat{\mathbf{x}}_\theta(\mathbf{z}_t; t) + \sqrt{\frac{\sigma_{t|s}^2 \sigma_s^2}{\sigma_t^2}} \epsilon. \quad (5)$$

## 4. Tetrahedral Representation Learning

**Tetra Convolution.** Our displacement and signed distance fields are not directly amenable to regular 3D convolutions due to varying neighborhoods and connectivity in the grid. However, the superimposed A15 lattice allows a collision-free spatial ordering of vertices within each neighborhood, and as such a well-defined, rigorous tetrahedral convolution. This is in contrast to graph convolutions that are invariant to the spatial configuration of the neighborhood, and unlike KPConv [45], our approach eliminates the need to search for the relevant points under the kernel and subsequent distance weighting. We define our unique ordering, a discrete binning of the local edge orientations, by iteratively clustering the set of all outgoing edges with  $k$ -means until we find a collision-free ordering, *i.e.* no edges within a neighborhood fall within the same bin. Interestingly, in practice our clustering approach always converges to a basis of at most  $m + 1$  reference directions, where  $m$  is the maximal neighborhood in the tetrahedral grid. In contrast to 3D voxel convolutions, the total number of basis directions is almost half the size (*e.g.* 15 compared to 26), highlighting one key ingredient to efficient learning. A concise description of our approach can be found in Sec. C.1.

With fixed ordering, it is straightforward to define the result of a tetrahedral convolution layer  $l$  at a given vertex



Figure 4. 3D shape interpolation. We first generate the leftmost and rightmost samples and save the noise applied in every diffusion step. Intermediate shapes are then generated by spherical linear interpolation of the noise.

$v_k$  as a weighted sum over itself and its neighborhood  $\mathcal{N}_{v_k}$  in layer  $(l - 1)$ :

$$\Phi_{v_k}^l = W_0 \Phi_{v_k}^{l-1} + \sum_{j=1}^{m+1} \mathbb{1}_{j \in \mathcal{N}_{v_k}} W_j \Phi_{v_j}^{l-1}, \quad (6)$$

where  $W_j$  are the weights of the kernel and  $\Phi_{v_i}^l$  the feature vector of  $v_i$  in layer  $l$ . As illustrated in Fig. 3a, the varying size of the neighborhood simply corresponds to zero padding the corresponding kernel. This layer is referred to as TetraConv. To fully exploit the power of convolutional learning, we need to define down- and upsampling operations on the tetrahedral grid. We construct tetrahedral tessellations of our cuboid  $\mathcal{T}$  of varying resolution and establish parent-child relations between vertices in adjacent hierarchy levels via  $k$ -nearest neighbor relations. As shown in Figure 3b, this enables flexible down- and upsampling rates corresponding to strided convolution and transposed convolution. In particular, the neighborhood in Eq. (6) gets replaced by the  $knn$ -neighborhood of the lower or higher tetrahedral resolution.

**Grid Pruning.** Like any volumetric tessellation, the tetrahedral grid is in most cases sparsely populated, reflecting the fact that only a small part of 3D space lies near an object surface. Unlike voxel-based convolutions, where only axis-parallel cropping is efficient (in particular limited to the bounding box), our tetrahedral formalism facilitates pruning in a more targeted manner. Deleting all unoccupied vertices and their corresponding connections translates to two simple operations: (1) unused vertices are completely removed by deleting the corresponding row in the unfolded kernel-data matrix and (2) removed connections lead to additional zero padding in affected rows. As a result, we can truncate our grid to the convex hull of all data used in a lossless manner. Additionally, training and inference speed and memory consumption is easily further enhanced by (lossy)

pruning vertices that are occupied only up to a user-defined number of times. A full description of the pruning methodology can be found in Sec. C.4.

**Tetrahedral Diffusion.** With all necessary building blocks at hand, we can now introduce our tetrahedral diffusion. We directly diffuse in deformable tetrahedral space, *i.e.* our basic input consists of  $N$  vertices with features  $\{s_v, \Delta_v\}$ , and the associated neighborhood relations. However, we can seamlessly extend the hybrid tetrahedral representation by any vertex feature vector, in particular color and texture information and without losing the differentiability of the marching tetrahedra algorithm. In particular, surface information like color is a convex combination of the corresponding tetrahedral vertex features. In our experiments we therefore directly diffuse SDF values, deformation vectors and color vectors per vertex, *i.e.*  $\{s_v, \Delta_v, c_v\}$ .

Our network largely adheres to the standard U-Vit architecture of many diffusion models [20], of course with the tetrahedral convolution operators introduced above, *i.e.*, residual convolution layers, with group normalization [49], SiLU activations [17] and attention layers in between. The entire network, hyperparameters and our tetrahedral marching extension are described in Sec. C.3.

## 5. Experiments

We now experimentally demonstrate the capabilities of TetraDiffusion. We train and evaluate our method on the classes *airplane*, *bike*, *car* and *chair* from the ShapeNet [5] dataset, using the official ShapeNet train/val/test split. Each shape is individually normalized to lie in  $[-1, 1]$ . Our network requires SDFs and displacement fields on a tetrahedral grid, *i.e.*, ShapeNet meshes have to be converted to that format. We adapt the rendering pipeline of [30] and fit each shape individually into the grid with a combination of rendering and volumetric losses. Similar to [26], the ground

Category	Method	1-NNA ↓		MMD ↓		COV ↑	
		CD	EMD	CD	EMD	CD	EMD
Airplane	GET3D [13]	93.1 ± 0.6	75.9 ± 1.6	0.42 ± 0.01	<u>0.52</u> ± 0.01	37.8 ± 1.2	44.0 ± 0.9
	MD [26]	89.2 ± 0.8	89.2 ± 0.7	0.64 ± 0.04	0.75 ± 0.01	32.5 ± 1.7	35.8 ± 1.0
	Ours	<b>71.9</b> ± 1.5	<b>68.3</b> ± 1.4	<b>0.30</b> ± 0.01	<b>0.49</b> ± 0.01	<b>48.2</b> ± 0.9	<b>47.8</b> ± 1.2
	Ours <sub>hr</sub>	<u>73.1</u> ± 1.1	<u>73.4</u> ± 1.4	<u>0.34</u> ± 0.01	0.52 ± 0.01	<u>44.5</u> ± 1.7	<u>46.5</u> ± 1.2
Bike	GET3D [13]	72.7 ± 3.0	68.8 ± 6.1	<u>1.65</u> ± 0.04	<u>1.18</u> ± 0.05	40.7 ± 4.8	47.8 ± 4.8
	MD [26]	<b>61.7</b> ± 5.3	<b>65.2</b> ± 6.0	<b>1.62</b> ± 0.13	1.18 ± 0.07	42.2 ± 5.3	49.3 ± 5.9
	Ours	<u>62.6</u> ± 4.7	<u>65.7</u> ± 5.6	1.71 ± 0.07	<b>1.17</b> ± 0.05	<u>45.7</u> ± 5.4	<u>52.7</u> ± 5.9
	Ours <sub>hr</sub>	65.9 ± 5.7	68.4 ± 5.1	1.82 ± 0.11	1.22 ± 0.06	<b>47.7</b> ± 4.9	<b>54.5</b> ± 5.1
Car	GET3D [13]	87.3 ± 0.7	73.6 ± 0.8	1.03 ± 0.01	0.72 ± 0.01	20.9 ± 1.4	34.2 ± 1.1
	MD [26]	68.6 ± 1.6	66.7 ± 2.5	0.93 ± 0.01	0.69 ± 0.01	35.1 ± 1.2	<b>42.3</b> ± 1.1
	Ours	<u>68.5</u> ± 0.9	<b>61.1</b> ± 1.4	<b>0.90</b> ± 0.01	<b>0.64</b> ± 0.01	<b>36.1</b> ± 1.6	<u>41.3</u> ± 1.6
	Ours <sub>hr</sub>	<b>67.1</b> ± 1.1	<u>61.4</u> ± 1.3	<u>0.91</u> ± 0.01	<u>0.65</u> ± 0.01	<u>35.6</u> ± 1.5	39.7 ± 1.3
Chair	GET3D [13]	76.4 ± 0.6	<u>72.9</u> ± 0.8	5.31 ± 0.04	<u>2.56</u> ± 0.01	31.8 ± 0.6	34.0 ± 0.4
	MD [26]	<u>73.0</u> ± 1.0	79.8 ± 0.9	<u>5.18</u> ± 0.12	2.79 ± 0.02	<u>38.2</u> ± 1.0	<u>35.2</u> ± 0.9
	Ours	<b>62.0</b> ± 0.6	<b>61.2</b> ± 0.9	<b>4.94</b> ± 0.11	<b>2.47</b> ± 0.03	<b>46.2</b> ± 0.6	<b>47.5</b> ± 0.8

Table 1. Generation metrics on ShapeNet classes airplane, bike, car and chair. MMD-CD is multiplied by  $\times 10^3$ , EMD by  $\times 10^2$ .

truth is created in two step procedure, fixing SDF values to  $\{-1, 1\}$ . For a comprehensive overview of the entire pre-processing protocol, please refer to the supplementary material.

## 5.1. Qualitative results

**Unconditional generation.** Figure 1 showcases a diverse array of randomly generated 3D shapes, demonstrating the high quality and level of detail of our model. Note the diversity of shapes within each class, and the intricate details like chains and brake discs on motorbikes or propellers and wing appendages on airplanes. The motorbikes nicely illustrate the model’s generative abilities: although the training set is small ( $\approx 200$  examples), the model goes beyond memorization and naive interpolation. It seamlessly blends parts of different training samples into plausible assemblies, and comes up with curious designs clearly not observed during training. It is noteworthy that, although further post-processing is a common practice in the context of 3D generative models, our generated shapes are not post-processed or cleaned in any way, as *e.g.* smoothing would remove fine structures and high-frequency details correctly synthesized by our model.

**Qualitative comparison.** Figure 5 compares TetraDiffusion against other recent mesh generators, namely GET3D [13] and MeshDiffusion (MD) [26]. We train all methods with resolution  $R = 128$  on the ShapeNet train-

ing split. Additionally, we also train a hi-res version of our model with  $R = 192$  denoted by *Ours<sub>hr</sub>*, which is not feasible for MD because it would exceed current hardware limitations on a single GPU (see also Tab. 2). The figure depicts examples from a large pool of generated shapes, matched across methods by finding the nearest neighbors to a given ground truth example from the test set. As general trends, we observe that (i) the GAN-based GET3D produces noisier shapes and has a tendency to hallucinate implausible shape details; (ii) TetraDiffusion tends to generate cleaner and more detailed shapes already at resolution  $R = 128$ : crease edges and small structures are crisper, while smooth surfaces have fewer bumps and holes; (iii) our hi-res version with  $R = 192$  clearly improves shape quality compared to the standard  $R = 128$ , supporting our claim that resolution is still a bottleneck: current 3D diffusion models run into hardware limits, and efficient use of memory and compute matters.

**Interpolation.** In Figure 4, we explore the latent shape space learned by our model. We can directly interpolate between two different shape instances using spherical interpolation to blend from start to end noise. Then, we feed the intermediate versions into the diffusion model to generate the corresponding meshes. The geometric integrity of the intermediate samples and the plausible, gradual transitions from start to end suggest that the model has indeed learned to disentangle objects along functionally meaningful dimensions,

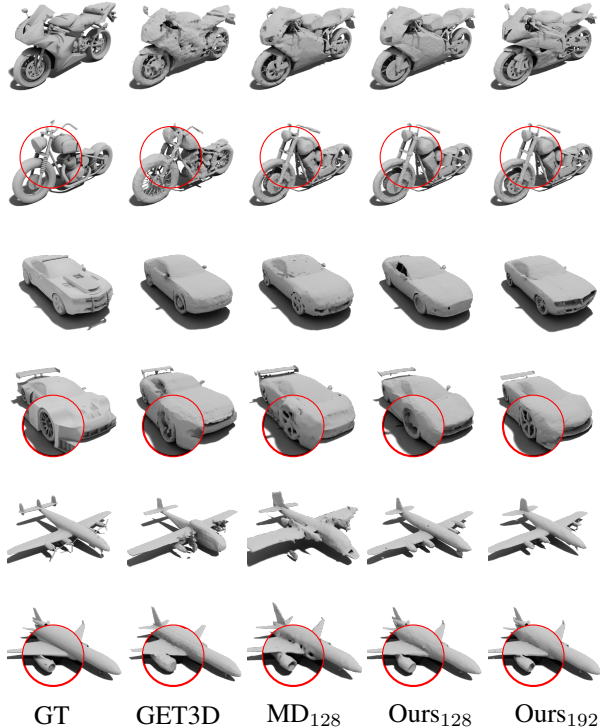


Figure 5. Comparison of different methods, red circles show enlarged highlights. Samples were collected by searching for the nearest neighbour to the ground truth. Ground truth samples are chosen from the test split. Best viewed when zoomed in.

and to represent them in terms of those components.

**Conditional Generation.** Our network can be seamlessly extended to conditional generation. We render multiple views for each ShapeNet shape and embed the images into CLIP space [35]. We expand our U-Net with additional cross-attention layers [6] and add the result to the output of the corresponding self-attention layer. We train our model conditioning on the shapes’ CLIP embeddings. At test time, we can then reconstruct faithful meshes from novel, unseen images by simply conditioning on the corresponding embedding. This effectively allows single-view reconstruction (SVR). We qualitatively show SVR results from RGB data in Fig. 6. Notably, the conditional model of TetraDiffusion, which is trained across all classes together, effectively discerns between diverse shapes and classes, and exhibits a strong adaptability to color variations.

## 5.2. Quantitative results

**Metrics.** We quantitatively evaluate our model in terms of *1-nearest neighbor accuracy* (1NNA), as proposed by Yang *et al.* [51], as well as minimum matching distance (MMD) and coverage (COV). All three latter metrics are computed

between the ground truth test set<sup>1</sup> and an equally large set of generated samples, and are based on pairwise distances between shapes. Since those distances are computed from point sets, we uniformly resample all (generated and ground truth) meshes into point clouds of size 2048 using the outer object surface only. Like [53], we compute all metrics based on both Earth Mover’s Distance (EMD) and Chamfer Distance (CD).

**1-NNA** measures the distributional discrepancy between two sets of point clouds: it finds the nearest neighbor for every generated sample and counts how often that nearest neighbor is another generated sample, respectively a ground truth sample. A value close to 50% is considered optimal: higher values mean that generated samples are far from the ground truth, indicating underfitting; lower values mean that the model mostly replicates ground truth samples, indicating overfitting. **MMD** measures the average distance from a generated sample to the nearest reference sample, as a proxy for fidelity to the ground truth shape space. **COV** quantifies what portion of reference samples are nearest neighbors to some generated sample, i.e., higher values mean that a larger part of the ground truth variability is covered by the generator.

We benchmark our model against the state-of-the-art 3D mesh generators, GET3D [13] and MeshDiffusion (MD) [26]. To get a meaningful and consistent comparison, we make sure that all models are evaluated with the same train/test split. To that end, we retrained all methods on the official ShapeNet training part. We sample 1000 shapes for each category and average ten runs with random splits equal the test set size. As demonstrated in Table 1, our method fares very well in the direct comparison. It achieves the best 1-NNA scores (i.e., it comes closest to 50) for 3 out of 4 object classes in terms of EMD and CD. We also achieve the highest COV scores in all cases, and the lowest MMD in all cases but one (CD for motorbikes).

Method	Training		Inference	
	GPU (GB)	Speed (it/s)	GPU (GB)	Speed (s/shape)
GET3D	13.3	0.10	11.3	0.83
MD	76.6	0.5	29.2 (22.6 <sup>†</sup> )	714.3 (526.3 <sup>†</sup> )
Ours*	12.0	2.8	7.4	3.4
Ours	20.8	1.0	9.7	11.2
Ours <sub>shr</sub> *	20.9	1.2	11.7	9.1
Ours <sub>shr</sub>	78.2	0.3	42.1	33.3

Table 2. Memory consumption and computing time of different generative shape models. <sup>†</sup> We implement 16-bit inference in MD for fair comparison. Our methods labelled with a \* are pruned versions, highlighting the efficiency boost of our tetrahedral formulation. Full details in Appendix.

<sup>1</sup>We follow literature [51, 53] and use the validation split of ShapeNet as the test set, which has not been used during training.



Figure 6. Conditional generation of 3D shapes. *TetraDiffusion* is conditioned on the CLIP embeddings of images in the wild during inference, while only trained on embeddings from rendered ShapeNet views. The shapes are displayed in matched pairs, with the upper image illustrating the condition and the lower image showcasing the corresponding generated mesh.

### 5.3. Efficiency

A central aspect of our approach is its efficiency. We argue that, despite the rapid development of GPU hardware, 3D generative models are at present held back by hardware limits, especially GPU memory (but also training time could become prohibitive when scaling current models up to industrial scale). In other words, a lighter and more efficient design makes 3D generative models not only faster and cheaper, but also yields results of higher quality.

By performing convolution natively on the tetrahedral grid, we can avoid overlaying a higher-resolution voxel grid as done, for instance, in *MeshDiffusion*. What is more, the voxel grid implies convolution kernels with at least  $3 \times 3 \times 3 = 27$ , whereas our operator works well with only 16 neighbors. This, in turn, makes it possible to increase the network capacity under the same hardware constraints. For instance *TetraDiffusion* can, due to its maller memory footprint, use 1028 feature channels in the bottleneck, and can also be run at higher resolution (see above).

Table 2 compares the computational demands of different 3D generative models. Our peak memory consumption at resolution  $R = 128$  (with batch size 1) is 20.8 GB, in contrast to *MeshDiffusion*'s 76.6 GB. Pruning the data cube as described in Section 4 further reduces memory usage to 12GB, without compromising prediction quality. Even at high resolution  $R = 192$ , and assuming that shape variability is so large that no significant pruning is possible, our model consumes less than 80 GB and can be run on a single high-end GPU. As a consequence, *TetraDiffusion* is also significantly faster. Inference time lies at about one shape per three seconds, getting close to GAN-based infer-

ence time and about  $200\times$  faster than *MeshDiffusion* on the same hardware.

Furthermore, the time-continuous formulation of our diffusion model provides the flexibility to vary sampling steps during inference. In other words, we are not constrained to a fixed number of steps, such as sampling with 1000 time steps. In our experimentation, detailed in the supplementary material, we explore the range of steps and demonstrate that we can successfully diffuse meshes within 32 steps without compromising quality.

## 6. Conclusion

We present *TetraDiffusion*, an innovative 3D diffusion framework capable of generating high-resolution, colored meshes with arbitrary topology and unprecedented resolution. To our knowledge, our work is the first 3D diffusion model that fully operates on a tetrahedral data structure, enabling highly efficient training and sampling processes. Through our experiments, we have showcased the ability of diffusion on the tetrahedral grid to synthesize diverse 3D shapes, incorporating attributes such as color and conditions based on CLIP features.

We believe a promising avenue for further exploration is to better leverage the extended differentiable tetrahedral marching algorithm and differentiable rendering [24, 30]. This approach aims to overcome the constraints of limited 3D assets and seamlessly integrate extensive 2D data into the framework. Moreover, *TetraDiffusion* is presently trained exclusively on objects. Nevertheless, the sparse nature of scenes represents a logical extension for our framework.



## References

- [1] Panos Achlioptas, Olga Diamanti, Ioannis Mitliagkas, and Leonidas Guibas. Learning representations and generative models for 3d point clouds. In *ICML*, 2018. 2
- [2] Andrew Brock, Theodore Lim, James M Ritchie, and Nick Weston. Generative and discriminative voxel modeling with convolutional neural networks. *arXiv preprint arXiv:1608.04236*, 2016. 2
- [3] Joan Bruna, Wojciech Zaremba, Arthur Szlam, and Yann LeCun. Spectral networks and locally connected networks on graphs. *arXiv preprint arXiv:1312.6203*, 2013. 2
- [4] Ruojin Cai, Guandao Yang, Hadar Averbuch-Elor, Zekun Hao, Serge Belongie, Noah Snavely, and Bharath Hariharan. Learning gradient fields for shape generation. In *ECCV*, 2020. 2
- [5] Angel X. Chang, Thomas Funkhouser, Leonidas Guibas, Pat Hanrahan, Qixing Huang, Zimo Li, Silvio Savarese, Manolis Savva, Shuran Song, Hao Su, Jianxiong Xiao, Li Yi, and Fisher Yu. ShapeNet: An information-rich 3d model repository. *arXiv preprint arXiv:1512.03012*, 2015. 5
- [6] Chun-Fu Richard Chen, Quanfu Fan, and Rameswar Panda. Crossvit: Cross-attention multi-scale vision transformer for image classification. In *ICCV*, pages 357–366, 2021. 7
- [7] Zhiqin Chen and Hao Zhang. Learning implicit fields for generative shape modeling. In *CVPR*, 2019. 2
- [8] Katherine Crowson. Clip guided diffusion hq 256x256. *Colab Notebook*. URL [https://colab.research.google.com/drive/12a\\_Wrfi2\\_gwwAuN3VvMTwVMz9TfqctNj](https://colab.research.google.com/drive/12a_Wrfi2_gwwAuN3VvMTwVMz9TfqctNj), 2021. 4
- [9] Prafulla Dhariwal and Alexander Nichol. Diffusion models beat GANs on image synthesis. In *NeurIPS*, 2021. 1
- [10] Crawford Doran, Athena Chang, and Robert Bridson. Isosurface stuffing improved: acute lattices and feature matching. In *ACM SIGGRAPH*, pages 1–1. 2013. 3, 2
- [11] Matheus Gadelha, Rui Wang, and Subhransu Maji. Multiresolution tree networks for 3d point cloud processing. In *ECCV*, 2018. 2
- [12] Jun Gao, Wenzheng Chen, Tommy Xiang, Alec Jacobson, Morgan McGuire, and Sanja Fidler. Learning deformable tetrahedral meshes for 3d reconstruction. In *NeurIPS*, 2020. 2
- [13] Jun Gao, Tianchang Shen, Zian Wang, Wenzheng Chen, Kangxue Yin, Daiqing Li, Or Litany, Zan Gojcic, and Sanja Fidler. Get3d: A generative model of high quality 3d textured shapes learned from images. *NeurIPS*, 35:31841–31854, 2022. 2, 6, 7, 12, 16
- [14] William Gao, April Wang, Gal Metzer, Raymond A Yeh, and Rana Hanocka. TetGAN: A convolutional neural network for tetrahedral mesh generation. *arXiv preprint arXiv:2210.05735*, 2022. 2, 3
- [15] Anchit Gupta, Wenhan Xiong, Yixin Nie, Ian Jones, and Barlas Oğuz. 3dgen: Triplane latent diffusion for textured mesh generation. *arXiv preprint arXiv:2303.05371*, 2023. 1, 3, 12
- [16] Nicholas Guttenberg. 17
- [17] Dan Hendrycks and Kevin Gimpel. Gaussian error linear units (GELUs). *arXiv preprint arXiv:1606.08415*, 2016. 5
- [18] Jonathan Ho and Tim Salimans. Classifier-free diffusion guidance. *arXiv preprint arXiv:2207.12598*, 2022. 2, 4
- [19] Jonathan Ho, Ajay Jain, and Pieter Abbeel. Denoising diffusion probabilistic models. In *NeurIPS*, 2020. 1
- [20] Emiel Hooeboom, Jonathan Heek, and Tim Salimans. simple diffusion: End-to-end diffusion for high resolution images. *arXiv preprint arXiv:2301.11093*, 2023. 3, 5, 13, 17
- [21] Alec Jacobson, Ilya Baran, Jovan Popovic, and Olga Sorkine. Bounded biharmonic weights for real-time deformation. *ACM ToG*, 30(4):78, 2011. 2
- [22] Diederik P Kingma, Tim Salimans, Ben Poole, and Jonathan Ho. Variational diffusion models. In *NeurIPS*, 2021. 3
- [23] Thomas N Kipf and Max Welling. Semi-supervised classification with graph convolutional networks. *arXiv preprint arXiv:1609.02907*, 2016. 2
- [24] Samuli Laine, Janne Hellsten, Tero Karras, Yeongho Seol, Jaakko Lehtinen, and Timo Aila. Modular primitives for high-performance differentiable rendering. *ACM Transactions on Graphics (TOG)*, 39(6):1–14, 2020. 8
- [25] Shanchuan Lin, Bingchen Liu, Jiashi Li, and Xiao Yang. Common diffusion noise schedules and sample steps are flawed. *arXiv preprint arXiv:2305.08891*, 2023. 17
- [26] Zhen Liu, Yao Feng, Michael J. Black, Derek Nowrouzezahrai, Liam Paull, and Weiyang Liu. Meshdiffusion: Score-based generative 3d mesh modeling. In *International Conference on Learning Representations*, 2023. 1, 2, 3, 5, 6, 7, 16
- [27] Calvin Luo. Understanding diffusion models: A unified perspective. *arXiv preprint arXiv:2208.11970*, 2022. 3
- [28] Shitong Luo and Wei Hu. Diffusion probabilistic models for 3d point cloud generation. In *CVPR*, 2021. 1, 3
- [29] Shentong Mo, Enze Xie, Ruihang Chu, Lewei Yao, Lanqing Hong, Matthias Nießner, and Zhenguo Li. Dit-3d: Exploring plain diffusion transformers for 3d shape generation. *arXiv preprint arXiv:2307.01831*, 2023. 3
- [30] Jacob Munkberg, Jon Hasselgren, Tianchang Shen, Jun Gao, Wenzheng Chen, Alex Evans, Thomas Müller, and Sanja Fidler. Extracting triangular 3d models, materials, and lighting from images. In *CVPR*, pages 8280–8290, 2022. 5, 8, 2, 12
- [31] Alex Nichol, Prafulla Dhariwal, Aditya Ramesh, Pranav Shyam, Pamela Mishkin, Bob McGrew, Ilya Sutskever, and Mark Chen. Glide: Towards photorealistic image generation and editing with text-guided diffusion models. *arXiv preprint arXiv:2112.10741*, 2021. 4
- [32] Gilles-Philippe Paillé, Nicolas Ray, Pierre Poulin, Alla Sheffer, and Bruno Lévy. Dihedral angle-based maps of tetrahedral meshes. *ACM ToG*, 34(4):1–10, 2015. 2
- [33] Songyou Peng, Chiyu Jiang, Yiyi Liao, Michael Niemeyer, Marc Pollefeys, and Andreas Geiger. Shape as points: A differentiable Poisson solver. In *NeurIPS*, 2021. 2, 3
- [34] Ethan Perez, Florian Strub, Harm De Vries, Vincent Dumoulin, and Aaron Courville. Film: Visual reasoning with a general conditioning layer. In *Proceedings of the AAAI conference on artificial intelligence*, 2018. 13
- [35] Alec Radford, Jong Wook Kim, Chris Hallacy, Aditya Ramesh, Gabriel Goh, Sandhini Agarwal, Girish Sastry,

- Amanda Askell, Pamela Mishkin, Jack Clark, et al. Learning transferable visual models from natural language supervision. In *ICML*, pages 8748–8763. PMLR, 2021. 7
- [36] Aditya Ramesh, Prfulla Dhariwal, Alex Nichol, Casey Chu, and Mark Chen. Hierarchical text-conditional image generation with CLIP latents. *arXiv preprint arXiv:2204.06125*, 2022. 1
- [37] Robin Rombach, Andreas Blattmann, Dominik Lorenz, Patrick Esser, and Björn Ommer. High-resolution image synthesis with latent diffusion models. In *CVPR*, 2022. 1, 2, 4
- [38] Olaf Ronneberger, Philipp Fischer, and Thomas Brox. U-net: Convolutional networks for biomedical image segmentation. In *MICCAI*, 2015. 2
- [39] Chitwan Saharia, William Chan, Saurabh Saxena, Lala Li, Jay Whang, Emily L Denton, Kamyar Ghasemipour, Raphael Gontijo Lopes, Burcu Karagol Ayan, Tim Salimans, et al. Photorealistic text-to-image diffusion models with deep language understanding. *Advances in Neural Information Processing Systems*, 35:36479–36494, 2022. 17
- [40] Tim Salimans and Jonathan Ho. Progressive distillation for fast sampling of diffusion models. *arXiv preprint arXiv:2202.00512*, 2022. 4
- [41] Tianchang Shen, Jun Gao, Kangxue Yin, Ming-Yu Liu, and Sanja Fidler. Deep marching tetrahedra: a hybrid representation for high-resolution 3d shape synthesis. In *NeurIPS*, 2021. 2, 3, 12
- [42] J Ryan Shue, Eric Ryan Chan, Ryan Po, Zachary Ankner, Jiajun Wu, and Gordon Wetzstein. 3d neural field generation using triplane diffusion. In *CVPR*, pages 20875–20886, 2023. 3
- [43] Jiaming Song, Chenlin Meng, and Stefano Ermon. Denoising diffusion implicit models. In *ICLR*, 2021. 1, 2, 4, 17
- [44] Yang Song, Jascha Sohl-Dickstein, Diederik P Kingma, Abhishek Kumar, Stefano Ermon, and Ben Poole. Score-based generative modeling through stochastic differential equations. *arXiv preprint arXiv:2011.13456*, 2020. 4
- [45] Hugues Thomas, Charles R Qi, Jean-Emmanuel Deschaud, Beatriz Marcotegui, François Goulette, and Leonidas J Guibas. KPConv: Flexible and deformable convolution for point clouds. In *ICCV*, 2019. 2, 4
- [46] Sinong Wang, Belinda Z Li, Madian Khabsa, Han Fang, and Hao Ma. Linformer: Self-attention with linear complexity. *arXiv preprint arXiv:2006.04768*, 2020. 13
- [47] Sven-Ake Wegner. Lecture notes on high-dimensional data. *arXiv preprint arXiv:2101.05841*, 2021. 10
- [48] Felix Wu, Amauri Souza, Tianyi Zhang, Christopher Fifty, Tao Yu, and Kilian Weinberger. Simplifying graph convolutional networks. In *ICML*, pages 6861–6871, 2019. 2
- [49] Yuxin Wu and Kaiming He. Group normalization. In *ECCV*, 2018. 5
- [50] Zhirong Wu, Shuran Song, Aditya Khosla, Fisher Yu, Linguang Zhang, Xiaoou Tang, and Jianxiong Xiao. 3d ShapeNets: A deep representation for volumetric shapes. In *CVPR*, 2015. 2
- [51] Guandao Yang, Xun Huang, Zekun Hao, Ming-Yu Liu, Serge Belongie, and Bharath Hariharan. PointFlow: 3d point cloud generation with continuous normalizing flows. In *ICCV*, 2019. 2, 7
- [52] Maciej Zamorski, Maciej Zieba, Piotr Klukowski, Rafał Nowak, Karol Kurach, Wojciech Stokowiec, and Tomasz Trzcziński. Adversarial autoencoders for compact representations of 3d point clouds. *CVIU*, 193:102921, 2020. 2
- [53] Xiaohui Zeng, Arash Vahdat, Francis Williams, Zan Gojcic, Or Litany, Sanja Fidler, and Karsten Kreis. LION: Latent point diffusion models for 3d shape generation. *arXiv preprint arXiv:2210.06978*, 2022. 1, 3, 7, 10
- [54] Linqi Zhou, Yilun Du, and Jiajun Wu. 3d shape generation and completion through point-voxel diffusion. In *ICCV*, 2021. 1, 3

# TetraDiffusion: Tetrahedral Diffusion Models for 3D Shape Generation

## Supplementary Material

<b>A Dataset preprocessing</b>	<b>2</b>
<b>B Additional qualitative results</b>	<b>3</b>
B.1. High resolution and inner structure . . . . .	3
B.2. Conditional generation . . . . .	4
B.3. Test time guidance . . . . .	4
B.4. Unconditional generation . . . . .	6
B.5. Interpolation . . . . .	10
<b>C Tetrahedral Diffusion</b>	<b>12</b>
C.1. Optimized Edge Binning Algorithm . . . . .	12
C.2. Tetrahedral marching extension . . . . .	12
C.3. Network . . . . .	13
C.4. Pruning . . . . .	14
<b>D Quantitative evaluation</b>	<b>14</b>
D.1. Metrics . . . . .	14
D.2. Quantitative results . . . . .	15
<b>E Ablations</b>	<b>17</b>
E.1. Step size . . . . .	17
E.2. Clipping and offset noise . . . . .	17

## A. Dataset preprocessing

We employ an isosurface stuffing algorithm with the A15 tile [10] to tessellate a cube  $[-1, 1]^3$  at the necessary grid resolutions using Quartet <https://github.com/crawforddoran/quartet>. Since our algorithm can handle arbitrary edge configurations, there is no need for post-processing non-symmetrical boundaries. In our experiments, we generate grids with tetrahedral resolutions of 32, 48, 64, 96, 128, and 192.

Our network requires SDF values, deformation vectors and color vectors. In order to convert meshes with possible texture maps, we adapt the optimization pipeline of [30] (*nvdiffrac* <https://github.com/NVlabs/nvdiffrac/>). In particular, we include per vertex color information and extend the marching tetrahedra algorithm to extract the corresponding surface color (see Sec. C.2). Originally, *nvdiffrac* jointly optimizes geometry and materials, stored in 2D textures, from multi-view object renderings. In our case, material information must be stored in the vertex features to jointly diffuse geometry and texture in a single U-Net, *i.e.* we implement a custom render function that additionally rasters and interpolates the vertex color information extracted from our extended marching tetrahedra. We iteratively optimize SDF value, deformation and color, starting from a random initialization, rendering random views uniformly around a sphere in each step. The vertex features are updated by backward propagation of different 2D and 3D loss functions, making use of the differentiable marching algorithm and differentiable rendering. In particular, we define the following total loss with respect to an optimizable mesh  $M_{\text{Opt}}$  extracted from the updated SDF, deformations and colors and the ground truth mesh  $M_{\text{Gt}}$ .

$$\mathcal{L}(M_{\text{Opt}}, M_{\text{Gt}}) = \lambda_1 \mathcal{L}_{\text{Img}} + \lambda_2 \mathcal{L}_{\text{Normal}} + \lambda_3 \mathcal{L}_{\text{Depth}} + \lambda_4 \mathcal{L}_{\text{Mask}} + \lambda_5 \mathbb{1}_{2^{nd}} \mathcal{L}_{\text{Laplace}} + \lambda_6 \mathcal{L}_{\text{Reg}}. \quad (7)$$

Similar to [26], the vertex features are updated in a two-stage procedure, each consisting of 5000 iterations in total. In a first step, we limit the deformation vector to a range of 0.45 of the grid resolution, which results in an increase in the number of vertices for the extracted mesh. A higher number of vertices allows better alignment of the ground truth shape in the second step, where we fix all SDF values to their respective sign, *i.e.*  $\text{SDF} \in \{-1, 1\}$ . We compensate for the restriction by increasing the range of the deformation vector to twice the grid resolution in the second step.

$\mathcal{L}_{\text{Img}}(M_{\text{Opt}}, M_{\text{Gt}})$ : We extract the two closest surfaces for each pixel in a raster using depth peeling, which allows us to optimize inner structure as well (see Sec. B.1). After interpolation and antialiasing, this gives us two pairs of RGB images  $\{(\text{Img}_1^{\text{gt}}, \text{Img}_1^{\text{opt}}), (\text{Img}_2^{\text{gt}}, \text{Img}_2^{\text{opt}})\}$  For which we compute gradients w.r.t. an L1-loss and  $\lambda_1 = 10$ .

$\mathcal{L}_{\text{Normal}}(M_{\text{Opt}}, M_{\text{Gt}})$ : Similar to the RGB images, we extract vertex (smooth shading) and face normals (flat shading) For both depth peels and compute gradients w.r.t. an L1-loss of ground truth and optimizable normals and  $\lambda_2 = 10$  For the first layer and  $\lambda_2 = 0.1$  For the second layer with slight abuse of notation. Smooth vertex normals are computed as the normalized average of the involved surface normals.

$\mathcal{L}_{\text{Depth}}(M_{\text{Opt}}, M_{\text{Gt}})$ : We compute normalized depth maps For both raster layers and compute the corresponding L1-loss. We weight the depth map with  $\lambda_3 = 100$ .

$\mathcal{L}_{\text{Mask}}(M_{\text{Opt}}, M_{\text{Gt}})$ : We render the silhouette of our shape For the first depth peel only, since the silhouette of the second layer does not provide much more information in general. Again, we use the L1-loss.

$\mathcal{L}_{\text{Chamfer}}(M_{\text{Opt}}, M_{\text{Gt}})$ : We compute the Chamfer distance w.r.t. to  $M_{\text{Gt}}$  and  $M_{\text{Opt}}$  and weight it with  $\lambda_4 = 1$ .

$\mathcal{L}_{\text{Laplace}}(M_{\text{Opt}}, M_{\text{Gt}})$ : To regularize the extracted triangular mesh, we add Laplacian smoothing using the weighted umbrella operator in the second stage of our optimization. The loss is attenuated over time.

$\mathcal{L}_{\text{Reg}}(M_{\text{Opt}}, M_{\text{Gt}})$ : To diminish floaters, we penalize sign flips in the SDF values with a cross-entropy loss defined over neighboring vertices, following [13, 30].

Additional to the aforementioned regularization loss, we encountered small floaters far away from the actual surface every now and then. In order to remove them, we simply compute the convex hull of our ground truth mesh and enforce all SDF values outside the hull to be positive.

## B. Additional qualitative results

### B.1. High resolution and inner structure

Our efficient architecture is capable of generating meshes in unprecedented resolution, capturing intricate details such as chains, fine rims, brake disks and brake handles. Importantly, these details are represented in the geometry of the mesh and not in texture maps. Diffusing per vertex texture information enforces the strong geometry. This capability is demonstrated in detail in Figure 7, where the visualizations showcase the model’s proficiency in reproducing realistic and fine-grained elements, contributing to the overall realism and quality of the generated shapes.

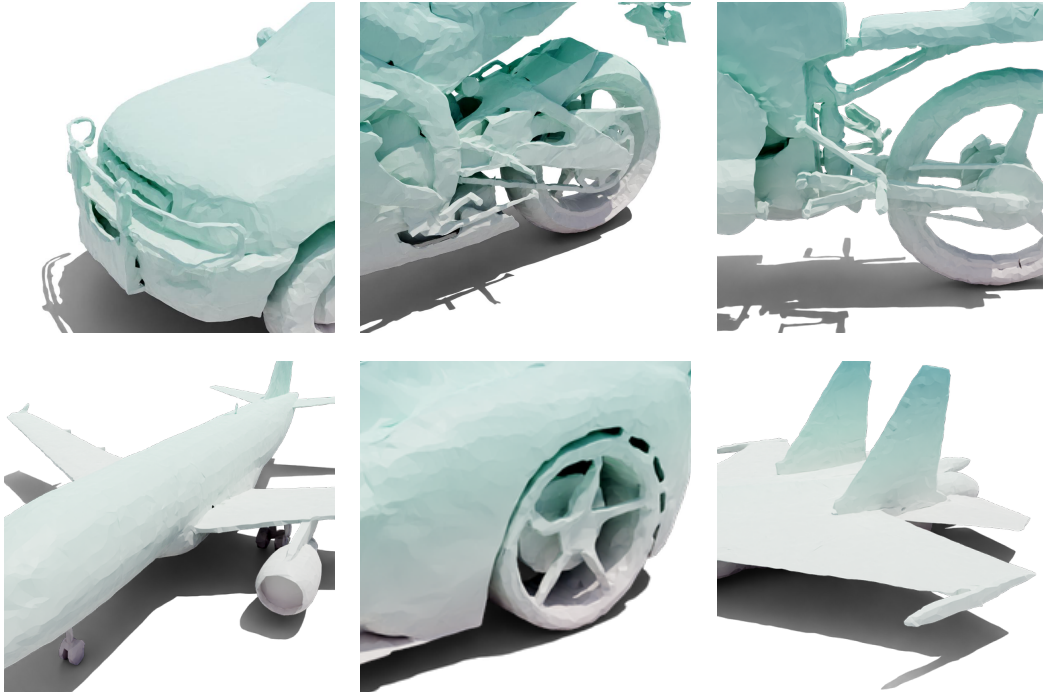


Figure 7. Details of generated meshes in high resolution

Additionally, our ground truth contains inner structure, as explained in Sec. A. Our models are able to generate consistent inner structure, *e.g.* seats, steering wheels or engines. Exemplary shapes are showcased in Figure 8.

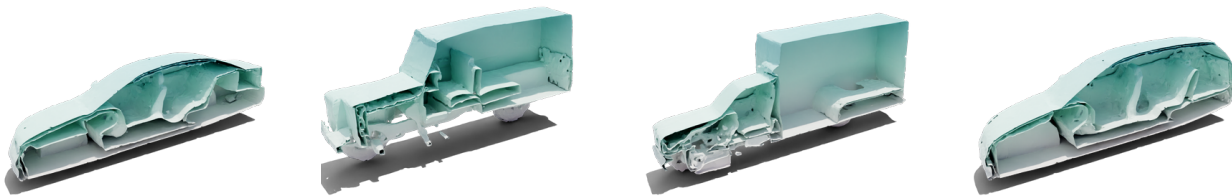


Figure 8. Examples of inner structure of our generated car meshes in high resolution



Figure 9. Shapes generated from a single view using our conditional model that was trained simultaneously on airplanes, bikes, cars, chairs and tables.

## B.2. Conditional generation

While our primary goal was not to develop a strong single-view reconstruction (SVR) model, TetraDiffusion can be easily extended to conditional generation. During training, we condition the U-Net on CLIP embeddings from multiple rendered views of ShapeNet meshes and use the CLIP feature of a single novel view during inference. Our approach requires only RGB images and offers flexibility with text embeddings. Note that we do not incorporate additional test time guidance. We depict samples in Figure 9.

## B.3. Test time guidance

Similar to classifier and classifier-free guidance [18, 37], we incorporate test time guidance, *i.e.* altering the mean prediction of the reverse diffusion process (*cf.* Equation (3)) with the gradient of a guiding task. *e.g.* In image diffusion, the guiding task can be a classifier  $p(y|z_t)$  trained to predict the correct class label  $y$  given the latent variable  $z_t$ . Instead of training an extra model or training a classifier-free conditional model, we explore the robustness of non-parametric guidance tasks, in the sense that no additional training is required, besides the unconditional model. In particular, we experiment with color and volumetric gradients making use of our fully differentiable mesh and rendering pipeline.

In order to guide the diffusion towards a specific colorized texture, we project the color in text form to its CLIP embedding and compare the embedding to image embeddings obtained by rendering multiple views of  $\hat{x}_\theta(z_t; t)$  in every step. The loss is computed as a spherical distance loss following [8]:

$$\mathcal{L}(e_{\text{color}}, e_{\text{render}}) = 2 \cdot \left[ \arcsin \left( \frac{\|e_{\text{color}} - e_{\text{render}}\|}{2} \right) \right]^2, \quad (8)$$

where  $e_{\text{color}} = \text{CLIP}(\text{"color"})$  is the CLIP embedding of a color in text form and  $e_{\text{render}} = \Phi(\theta(z_t; t))$  is a rendered view of the mesh extracted from  $\hat{x}_\theta(z_t; t)$  with our extended marching tetrahedra algorithm.

Additionally, we may influence the volume of the diffused mesh by simply pushing the bounding box of the extracted mesh towards smaller or larger extents.

Of course these guidance tasks are orthogonal to each other and can be combined to change volume and color at the same time due to our somewhat disentangled representation. We depict guided samples in Figure 10. As pointed out by [31], this

simple approach may result in slightly deteriorate results as the renderings of noisy meshes are out of distribution For the CLIP model.

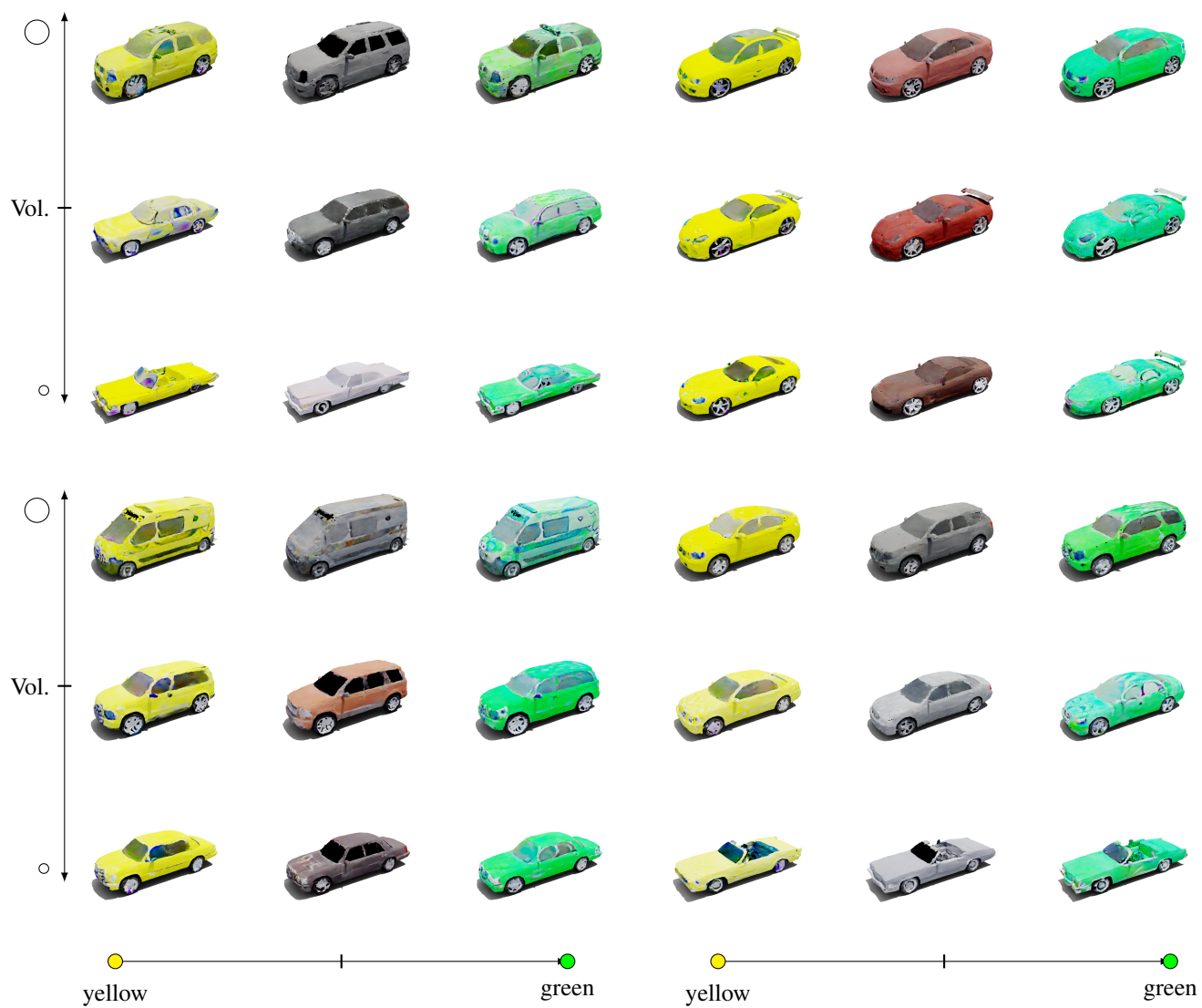


Figure 10. Exemplary results using text and volume guidance using only the unconditional model.

#### B.4. Unconditional generation

Additional renderings of shapes generated with TetraDiffusion can be found in Fig. 14, Fig. 16, Fig. 12, Fig. 17, Fig. 13, Fig. 15 and Fig. 11. TetraDiffusion consistently produces high-quality results with substantial diversity. Notably, even in low data regimes such as the ShapeNet bike class, our model learns a meaningful manifold and reliably interpolates novel shapes.



Figure 11. A random selection of cars generated in high resolution.



Figure 12. A random selection of cars generated in our standard resolution.





Figure 13. A random selection of airplanes generated in high resolution.



Figure 14. A random selection of airplanes generated in our standard resolution.



Figure 15. A random selection of motorbikes generated in high resolution.



Figure 16. A random selection of motorbikes generated in standard resolution.



Figure 17. A random selection of chairs generated in standard resolution.

## B.5. Interpolation

Here, we perform shape interpolation, a common task in generative models. We smoothly transform one shape to another by interpolating along the noise vectors. Let the noise vector of shape  $i$  be  $z_{i,t}$  at time step  $t$ . Common in 2D diffusion is to simply linearly interpolate between two noise vectors  $z_{1,t}$  and  $z_{2,t}$ . However, similar to [53], we find that a simple convex combination of the noise vectors leads to poor results in 3D, *e.g.* holes, deformations or corrupted colors. The authors of [53] provide a precise explanation: due to the high dimensionality of the input space, the noise samples almost certainly lie on a thin spherical shell according to the Gaussian annulus theorem. Therefore, they propose to use a square root-based interpolation, in order to stay within the training set learned by the model.

Another, simpler reason is that the linear interpolation of two standard Gaussians is not a standard Gaussian anymore. For  $i = 1, 2$  let  $X_i \sim \mathcal{N}(0, I)$  be independent Gaussian random variables and  $\lambda_1 = 1 - \lambda_2$ ,  $\lambda_i \in [0, 1]$ . Then  $X := \lambda_1 X_1 + \lambda_2 X_2 \sim \mathcal{N}(0, \sigma^2 := \lambda_1^2 + \lambda_2^2)$ , *i.e.* in particular  $\sigma^2 = 1 \iff \lambda_i = 1$  (see [47] For a more general proof). In particular, we end up with a non-isotropic Gaussian between the end values. To have isotropic Gaussian samples in between, one needs to take the square root of the interpolation weights, as proposed by [53].

Additionally, we found that morphing with the square root-based interpolation resulted in sudden jumps between shapes. Instead, we have used spherical interpolation (Slerp) as defined in the following:

$$\hat{z}_{t,k} := \text{Slerp}(z_{t,0}, z_{t,1}; k) = \frac{\sin[(1-k)\Omega]}{\sin \Omega} z_{t,0} + \frac{\sin [k\Omega]}{\sin \Omega} z_{t,1}, \quad (9)$$

where  $\Omega$  is the subtended angle between the arc that is spanned by each  $z_{t,0}$  and  $z_{t,1}$  on the sphere and  $k \in [0, 1]$ . In order to interpolate between two shapes we interpolate all noise vectors using equation Eq. (9) along the trajectory, resulting in smooth interpolations as we are explicitly moving along the arc on the high dimensional sphere. See Figure 18 for various interpolations of airplanes, cars and chairs.



Figure 18. Exemplary shape interpolation. We first generate the leftmost and rightmost samples and save the noise applied in every diffusion step. Intermediate shapes are then generated by spherical linear interpolation of the noise.

## C. Tetrahedral Diffusion

### C.1. Optimized Edge Binning Algorithm

---

**Algorithm 1** Optimized Binning for Tetrahedral Grid Convolution

---

**Require:** Grid vertices  $V$ , cluster count  $k = m + 1$ , max number of iterations  $n$

**Ensure:** Ordered edge sets for each vertex

```

1: Initialize  $k$ -means with  $k$  clusters
2: for each vertex  $v \in V$  do
3:   Collect outgoing edges  $E_v$  centered at  $v$ 
4: end for
5: Cluster all edges  $E = \bigcup_v E_v$  into  $k$  groups
6: for each vertex  $v \in V$  do
7:   for each edge  $e \in E_v$  do
8:     Assign  $e$  to closest cluster based on cosine similarity
9:   end for
10:  Sort assigned edges of  $v$  based on cluster order
11: end for
12: Check for collisions in edge assignments
13: if collisions exist then
14:   if current iteration  $< n$  then
15:     repeat clustering and sorting
16:   else
17:     Increment  $k$  and repeat clustering and sorting
18:   end if
19: end if

```

---

As already outlined in the main paper, the hybrid tetrahedral representation cannot be manipulated with regular grid-based convolution, since the neighborhood of a vertex in the grid can vary. However, even though the tetrahedral grid initialized with Quartet is relatively regular, it is not straightforward to establish a discrete binning of the local edge orientations that would define a unique, collision-free ordering. To resolve this we propose to globally optimize the binning in such a way that a unique ordering is ensured, see Alg. 19

1. Collect the set of outgoing edges at all vertices of the (undeformed) grid, center them in one point, and cluster them into  $k = m + 1$  groups with  $k$ -means. The cluster centers serve as a global basis of reference directions.
2. Arrange the basis vectors in a fixed order. At every vertex, assign the outgoing edges to basis vectors according to the cosine similarity to obtain a spatially meaningful ordering For convolution.
3. If, at any vertex, the binning would lead to a collision, increment  $k$  to expand the number of basis vectors and repeat clustering and assignment.

In practice, we have never seen a case where a collision-free basis needed more than  $m + 1$  reference directions.

### C.2. Tetrahedral marching extension

The differentiable Marching Tetrahedra algorithm has been popularized by [41] and utilized in various works [13–15, 30]. Similar to the Marching Cube scheme, that algorithm individually inspects every tetrahedron to determine the surface topology. Whenever the sign of the SDF changes within a tetrahedron, the surface must pass through it and one can extract the corresponding triangle by interpolating the vertex positions:

$$v_{ab} = \frac{(v_a + \Delta_{v_a}) \cdot s_b - (v_b + \Delta_{v_b}) \cdot s_a}{s_b - s_a}, \quad (10)$$

where  $s_x$  is the SDF value of vertex  $x$  and  $\Delta_{v_x}$  its corresponding deformation vector,  $x \in \{a, b\}$ .

In our case, we not only want to diffuse untextured meshes, but include texture information without using multiple networks. Luckily, extending the Marching Tetrahedra algorithm to extract any mesh vertex feature is as simple as adding features in the parenthesis in Eq. (10), *i.e.*  $(v_x + \Delta_{v_x} + c_{v_x} + \dots + *_{v_x})$ , where  $c_{v_x}$  is *e.g.* color information.

### C.3. Network

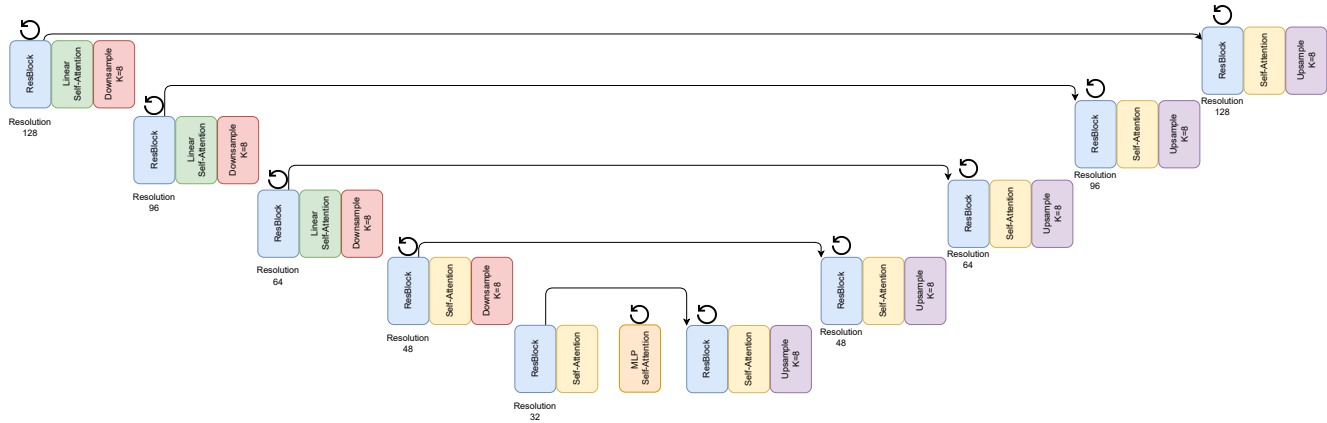


Figure 19. Schematic of our U-ViT with 128 Resolution. Every ResBlock, Downsample and Upsample contain TetraConv blocks.

The general structure of our network is depicted in Fig 19. Our standard network (resolution 128) has five encoder stages with  $\{128, 128, 128, 512, 1024\}$  channels. Each stage consists of two residual blocks with tetrahedral convolutions followed by a linear attention layer [46]. In the last two stages the linear attention layers are substituted with regular self-attention layers. Our bottleneck comprises four Transformer blocks, each with self-attention followed by a Multilayer Perceptron (MLP). The time parameter  $t$  is embedded via feature modulation [34]. Our downsampling rate is 0.75, e.g. going from a 128-cube to a 96-cube. The lowest resolution is 32. In the following, we list the most important training parameters.

```

cube_res: [128, 96, 64, 48, 32]
first_channel: 128
vit_depth: 4
num_blocks: [2, 2, 2, 2, 2]
channel_multiplier: [1, 1, 1, 4, 8]
dropout: [0.0, 0.0, 0.0, 0.1, 0.1]
linear_attentions: [True, True, True, True, False]
attentions: [False, False, False, False, True]
group_norm_groups: 32
knn_up_downsample: 8
ema_decay: 0.995
lr: 1.e-4

```

Differently, for our high resolution network, *i.e.* a resolution of 192, we directly downsample from 192 to 128, as to reduce memory requirements. However, to increase information flow, we use a nearest neighborhood size of 16 instead of 8 when defining the downsampling operation. Additionally, we only use linear attention layers to accelerate sampling. We have not encountered a loss in performance using the higher downsampling rate and only linear attention layers. We only list parameters that have changed below.

```

cube_res: [192, 128, 64, 48, 32]
channel_multiplier: [1, 1, 2, 4, 6]
linear_attentions: [True, True, True, True, True]
attentions: [False, False, False, False, False]
knn_up_downsample: 16

```

We have found noise shift to be an important parameter when diffusing high resolution shapes. Following [20], we shift the noise scheduler by a factor of  $\frac{128}{32} = 4$ , which increases the noise level throughout the diffusion processes. We hypothesize

that the combination of noise shift,  $\nu$ -parametrization and the time-continuous formulation allows us to sample high quality shapes within 24 steps.

### C.4. Pruning

Similar to other volumetric representations, the tetrahedral grid is typically sparsely populated. This reflects the observation that only a small portion of 3D space is in close proximity to an object’s surface. However, our fully tetrahedral formulation allows us to alleviate this disadvantage, boosting computational efficiency. To do so, we systematically remove sections of the grid that are infrequently or never used. Unlike regular 3D convolutions, which permit only axis-parallel cropping, our tetrahedral convolutions enable more precise and efficient elimination. In data space, *i.e.* in the first layer of our architecture, unused vertices are directly removed from the input grid, with subsequent updating of the vertices’ neighborhoods. On the contrary, this procedure becomes notably intricate in the lower layers. Here, not only must we update the vertices, neighborhoods, and tetrahedrons of the remaining vertices from the preceding layer, but we also need to ensure that vertices within the current layer’s receptive field from those layers are preserved as downsampling is defined over nearest neighbors. Our proposed methodology initiates at the data level, applying a global occupancy mask (indicating vertex usage with 1 or 0). We propagate this mask to the lower resolution grids using our TetraConv and downsampling layers. Then, we iteratively process each level, removing unused connections (responses are all zero) and updating affected vertices, including their neighborhoods and tetrahedral indices. Conceptually, deleting a vertex corresponds to removing a row, and removing an edge equates to inserting a zero in a cell within the unfolded data matrix, as depicted in Figure 3. This entire refinement process is executed once, requiring only a few seconds, and is depending on the data set and the specific network configuration to be trained. It’s important to note that the pruning of vertices and connections in our methodology is non-lossy, meaning it neither compromises network performance nor results in data loss. This technique is particularly beneficial for high-resolution data, which is often sparsely populated. We can significantly accelerate both training and inference times without sacrificing information. In our experiments, the proportion of utilized data ranged from 8% (when trained on a single class) to 82% (when training across all available classes, such as airplanes, bikes, cars, and chairs).

## D. Quantitative evaluation

### D.1. Metrics

We evaluate our model in terms of 1-nearest neighbor accuracy (1NNA), minimum matching distance (MMD) and coverage (COV). All metrics compare a set of reference point clouds  $S_r$  to a generated set of point clouds  $S_g$ . Importantly, the sets should be of same size, *i.e.*  $|S_r| = |S_g|$ . In all our experiments, the individual point clouds are of size 2048.

**1NNA** measures diversity and quality of the generated samples. It is defined as the leave-one-out accuracy of the 1-nearest neighbor classifier over the union of the two sets. In particular, a value of 50% is considered optimal: half of the generated samples are closest to a reference sample and the other half is closest to a generated sample. Values above 50% correlate with underfitting - generated samples are further away from the ground truth - and values below 50% coincide with overfitting. The score can be computed with the following equation:

$$\text{1NNA}(S_g, S_r) = \frac{\sum_{x \in S_g} \mathbb{1}[\mathcal{N}_x \in S_g] + \sum_{y \in S_r} \mathbb{1}[\mathcal{N}_y \in S_r]}{|S_r| + |S_g|}, \quad (11)$$

where  $\mathcal{N}_x$  is the nearest neighbor of  $x$  in the set  $S_r \cup S_g - \{x\}$ . The nearest neighbor can be computed in terms of Chamfer Distance (CD) or Earth Mover Distance (EMD).

**MMD** computes the minimal distance between each reference sample and the nearest generated sample using CD or EMD and averages the score over the reference set:

$$\text{MMD}(S_g, S_r) = \frac{1}{|S_r|} \sum_{y \in S_r} \min_{x \in S_g} D(x, y), \quad (12)$$

where  $D(\cdot, \cdot)$  is either CD or EMD.



**COV** quantifies the portion of reference samples that are matched to a generated samples. Higher values indicate diversity in the generative model. Mathematically, this translates to

$$\text{COV}(S_g, S_r) = \frac{1}{|S_g|} |\{\arg \min_{y \in S_r} D(x, y) | x \in S_g\}|, \quad (13)$$

where  $D(\cdot, \cdot)$  is either CD or EMD.

## **D.2. Quantitative results**

We provide additional quantitative comparisons using different sampling strategies and reference datasets, namely sampling point clouds with inner structure (Tab. 5) and a reference set sampled from our ground truth meshes with inner (Tab. 3) and only outer surface (Tab. 4).

Category	Method	1-NNA ↓		MMD ↓		COV ↑	
		CD	EMD	CD	EMD	CD	EMD
Airplane	GET3D [13]	93.51 ± 0.48	76.31 ± 0.86	0.43 ± 0.00	0.57 ± 0.00	34.86 ± 0.89	41.14 ± 1.17
	MD [26]	89.6 ± 0.98	87.56 ± 1.25	0.64 ± 0.03	0.81 ± 0.02	33.01 ± 1.67	35.48 ± 1.70
	Ours	<b>73.38</b> ± 1.21	<b>63.51</b> ± 1.89	<b>0.31</b> ± 0.01	<b>0.51</b> ± 0.01	<b>46.22</b> ± 1.41	<b>51.75</b> ± 1.07
Bike	GET3D [13]	72.98 ± 3.01	59.85 ± 5.58	1.48 ± 0.04	<b>1.19</b> ± 0.04	41.01 ± 5.26	48.18 ± 5.92
	MD [26]	<b>65.25</b> ± 4.92	61.31 ± 6.19	<b>1.44</b> ± 0.11	1.22 ± 0.07	42.63 ± 5.21	<b>55.35</b> ± 5.39
	Ours	65.96 ± 4.53	<b>57.22</b> ± 5.71	1.55 ± 0.06	1.23 ± 0.06	<b>46.16</b> ± 5.20	53.74 ± 4.90
Car	GET3D [13]	96.96 ± 0.36	90.21 ± 0.76	1.50 ± 0.01	1.08 ± 0.02	9.66 ± 0.52	19.0 ± 0.90
	MD [26]	74.8 ± 1.59	67.39 ± 1.09	1.14 ± 0.01	0.80 ± 0.01	34.01 ± 0.59	41.12 ± 1.47
	Ours	<b>69.08</b> ± 1.37	<b>59.00</b> ± 1.91	<b>1.08</b> ± 0.01	<b>0.74</b> ± 0.01	<b>36.68</b> ± 1.45	<b>47.59</b> ± 1.80
Chair	GET3D [13]	78.22 ± 0.49	72.35 ± 0.67	5.13 ± 0.03	2.59 ± 0.01	31.59 ± 0.46	37.04 ± 0.47
	MD [26]	73.21 ± 0.89	72.85 ± 0.70	5.01 ± 0.09	2.77 ± 0.05	38.95 ± 0.89	41.71 ± 1.20
	Ours	<b>68.18</b> ± 0.86	<b>65.52</b> ± 1.14	<b>4.72</b> ± 0.09	<b>2.53</b> ± 0.02	<b>42.08</b> ± 0.84	<b>47.64</b> ± 0.98

Table 3. Generation metrics on ShapeNet classes airplane, bike, car and chair, sampling inner and outer structure. Reference dataset was sampled from our ground truth. MMD-CD is multiplied by  $\times 10^3$ , EMD by  $\times 10^2$ .

Category	Method	1-NNA ↓		MMD ↓		COV ↑	
		CD	EMD	CD	EMD	CD	EMD
Airplane	GET3D [13]	93.44 ± 0.80	70.51 ± 1.51	0.43 ± 0.01	0.49 ± 0.00	36.81 ± 1.29	47.60 ± 1.17
	MD [26]	89.84 ± 0.70	87.04 ± 0.88	0.63 ± 0.04	0.71 ± 0.02	33.25 ± 1.23	34.02 ± 1.48
	Ours	<b>72.26</b> ± 1.76	<b>63.27</b> ± 1.61	<b>0.30</b> ± 0.00	<b>0.46</b> ± 0.00	<b>47.75</b> ± 1.00	<b>48.94</b> ± 0.97
Bike	GET3D [13]	73.79 ± 3.63	66.87 ± 5.48	1.66 ± 0.03	<b>1.10</b> ± 0.04	39.29 ± 4.81	50.10 ± 4.89
	MD [26]	<b>63.43</b> ± 3.46	<b>61.92</b> ± 6.82	<b>1.59</b> ± 0.15	1.11 ± 0.07	42.42 ± 5.51	52.12 ± 6.86
	Ours	64.95 ± 5.45	62.47 ± 6.75	1.72 ± 0.07	1.13 ± 0.06	<b>45.35</b> ± 6.29	<b>54.34</b> ± 5.62
Car	GET3D [13]	86.50 ± 0.44	70.57 ± 1.61	1.02 ± 0.00	0.59 ± 0.00	20.41 ± 0.98	38.05 ± 1.68
	MD [26]	68.40 ± 1.36	60.97 ± 1.58	0.93 ± 0.01	0.57 ± 0.00	34.24 ± 1.43	44.53 ± 1.60
	Ours	<b>65.93</b> ± 1.13	<b>53.40</b> ± 1.02	<b>0.89</b> ± 0.01	<b>0.55</b> ± 0.00	<b>35.36</b> ± 0.93	<b>45.07</b> ± 1.05
Chair	GET3D [13]	76.89 ± 0.75	70.38 ± 0.66	5.29 ± 0.02	2.37 ± 0.01	31.90 ± 0.46	37.55 ± 0.70
	MD [26]	72.22 ± 0.86	80.09 ± 0.62	5.12 ± 0.08	2.64 ± 0.04	38.82 ± 1.20	38.02 ± 0.58
	Ours	<b>61.28</b> ± 0.95	<b>59.58</b> ± 0.77	<b>4.93</b> ± 0.10	<b>2.36</b> ± 0.03	<b>46.30</b> ± 0.41	<b>48.83</b> ± 0.90

Table 4. Generation metrics on ShapeNet classes airplane, bike, car and chair. Only the outer surface was sampled. Reference dataset was sampled from our ground truth. MMD-CD is multiplied by  $\times 10^3$ , EMD by  $\times 10^2$ .

Category	Method	1-NNA ↓		MMD ↓		COV ↑	
		CD	EMD	CD	EMD	CD	EMD
Airplane	GET3D [13]	94.36 ± 0.47	87.30 ± 0.89	0.43 ± 0.00	0.71 ± 0.01	37.48 ± 0.82	35.33 ± 1.49
	MD [26]	89.73 ± 1.27	89.4 ± 0.78	0.65 ± 0.04	0.91 ± 0.02	34.25 ± 1.54	35.23 ± 1.53
	Ours	<b>80.15</b> ± 1.14	<b>77.35</b> ± 1.18	<b>0.33</b> ± 0.01	<b>0.62</b> ± 0.01	<b>45.58</b> ± 1.63	<b>45.65</b> ± 1.19
Bike	GET3D [13]	74.95 ± 2.95	68.19 ± 3.77	1.46 ± 0.04	1.37 ± 0.04	35.88 ± 4.91	40.49 ± 4.80
	MD [26]	<b>65.39</b> ± 4.76	<b>61.42</b> ± 6.48	<b>1.41</b> ± 0.11	<b>1.33</b> ± 0.08	<b>41.96</b> ± 5.40	<b>47.65</b> ± 4.91
	Ours	66.57 ± 5.38	64.17 ± 7.04	1.53 ± 0.06	1.37 ± 0.08	<b>41.96</b> ± 6.18	44.61 ± 5.47
Car	GET3D [13]	97.16 ± 0.31	90.80 ± 0.69	1.47 ± 0.02	1.13 ± 0.01	10.57 ± 0.44	18.18 ± 0.97
	MD [26]	<b>73.01</b> ± 1.72	65.28 ± 1.38	1.12 ± 0.01	0.86 ± 0.01	34.69 ± 1.86	41.82 ± 2.35
	Ours	73.35 ± 1.36	<b>63.04</b> ± 1.80	<b>1.08</b> ± 0.00	<b>0.83</b> ± 0.01	<b>35.20</b> ± 1.60	<b>42.33</b> ± 1.25
Chair	GET3D [13]	78.26 ± 0.43	73.62 ± 0.65	5.11 ± 0.02	2.64 ± 0.01	32.33 ± 0.56	36.28 ± 0.63
	MD [26]	72.43 ± 0.96	72.13 ± 1.60	4.98 ± 0.08	2.79 ± 0.05	38.60 ± 0.81	41.66 ± 0.90
	Ours	<b>67.09</b> ± 0.71	<b>66.69</b> ± 0.97	<b>4.76</b> ± 0.09	<b>2.58</b> ± 0.02	<b>41.43</b> ± 0.60	<b>47.07</b> ± 1.53

Table 5. Generation metrics on ShapeNet classes airplane, bike, car and chair, sampling inner and outer structure. Reference dataset was sampled from ShapeNet ground truth. MMD-CD is multiplied by  $\times 10^3$ , EMD by  $\times 10^2$ .

## E. Ablations

### E.1. Step size

Treating time as continuous rather than discrete allows us to vary sampling steps during inference without relying on DDIM sampling strategies [43]. Here, we quantitatively evaluate the range of steps needed in *TetraDiffusion* to generate diverse and high quality meshes. The metrics for steps 24, 32, 48, 64, 96 and 128 can be found in Table 6. Overall, the model tends to perform equally well starting from 32 time steps.

Category	Step size	1-NNA ↓		MMD ↓		COV ↑	
		CD	EMD	CD	EMD	CD	EMD
Airplane	24	78.27 ± 1.17	74.37 ± 1.20	0.32 ± 0.01	0.53 ± 0.01	38.96 ± 0.99	40.64 ± 1.41
	32	74.84 ± 0.95	72.17 ± 1.59	0.32 ± 0.01	0.52 ± 0.01	43.01 ± 0.75	43.80 ± 1.70
	48	73.51 ± 0.51	70.89 ± 1.35	0.32 ± 0.01	0.51 ± 0.01	46.96 ± 1.11	44.44 ± 1.99
	64	72.05 ± 1.21	<b>68.37</b> ± 1.30	<b>0.30</b> ± 0.01	<b>0.49</b> ± 0.00	47.56 ± 0.67	46.86 ± 1.07
	96	72.27 ± 1.12	72.89 ± 1.14	0.31 ± 0.01	0.51 ± 0.01	47.06 ± 1.40	46.07 ± 0.62
	128	<b>71.41</b> ± 2.07	69.28 ± 1.89	0.31 ± 0.01	0.50 ± 0.01	<b>48.10</b> ± 2.43	<b>47.41</b> ± 0.68
Car	24	73.31 ± 1.15	68.43 ± 1.75	0.92 ± 0.01	<b>0.63</b> ± 0.01	35.14 ± 0.86	<b>44.4</b> ± 1.47
	32	67.91 ± 1.03	61.8 ± 1.06	0.91 ± 0.01	<b>0.63</b> ± 0.02	<b>37.71</b> ± 0.95	44.29 ± 1.32
	48	68.97 ± 1.09	<b>60.43</b> ± 1.60	0.90 ± 0.01	<b>0.63</b> ± 0.02	36.40 ± 2.16	42.46 ± 1.73
	64	68.20 ± 0.99	61.71 ± 1.90	0.90 ± 0.01	<b>0.63</b> ± 0.01	35.26 ± 1.15	42.23 ± 1.75
	96	67.77 ± 1.08	60.89 ± 0.76	0.91 ± 0.01	0.66 ± 0.01	33.77 ± 1.02	42.57 ± 1.83
	128	<b>66.89</b> ± 1.22	60.49 ± 1.28	<b>0.89</b> ± 0.00	0.65 ± 0.00	35.60 ± 0.52	40.57 ± 2.12
Chair	24	70.85 ± 1.05	69.42 ± 0.68	5.47 ± 0.05	2.69 ± 0.02	40.58 ± 0.48	43.85 ± 0.80
	32	66.65 ± 0.38	63.98 ± 1.30	5.05 ± 0.08	2.56 ± 0.03	43.99 ± 0.64	45.34 ± 0.37
	48	64.40 ± 0.39	62.93 ± 0.46	5.18 ± 0.06	2.58 ± 0.02	44.29 ± 0.32	47.73 ± 0.42
	64	<b>61.94</b> ± 0.58	<b>60.52</b> ± 0.35	4.96 ± 0.06	2.47 ± 0.02	46.18 ± 0.72	47.64 ± 0.81
	96	63.48 ± 1.21	61.72 ± 1.11	4.89 ± 0.01	<b>2.46</b> ± 0.02	<b>46.36</b> ± 0.54	47.52 ± 0.97
	128	62.51 ± 0.58	62.51 ± 0.77	<b>4.85</b> ± 0.05	2.48 ± 0.02	45.74 ± 0.49	<b>48.05</b> ± 1.20

Table 6. Ablation over step size on ShapeNet classes airplane, bike, car and chair, sampling only outer structure. Reference dataset was sampled from ShapeNet ground truth. MMD-CD is multiplied by  $\times 10^3$ , EMD by  $\times 10^2$ .

### E.2. Clipping and offset noise

Additionally, we ablate two orthogonal inference strategies, namely clipping  $\hat{x}_\theta(\mathbf{z}_t; t)$  to the data range along the reverse diffusion chain and varying the offset noise [16]. Clipping the prediction in x-space is often found in codebases but often not emphasized [20, 39]. As  $\hat{x}_\theta(\mathbf{z}_t; t)$  is iteratively used in ancestral sampling, not clipping can be seen as a train-test mismatch and may lead to deteriorate performance [39].

An interesting observation was made in [16, 25]. Diffusion models tend to generate images with medium brightness due to the discrepancy between training and inference signal-to-noise ratio. This becomes even more apparent in the high resolution regime as low frequency features are often not completely removed during the forward process. Reversely, the long wavelength features of the Gaussian noise at the start of the reverse diffusion process are least likely to be destructed, which forces images to respect the average value, the longest wavelength. A simple, yet effective solution is proposed by [16]: randomizing the zero-frequency component of the noise by adding single independent and identically distributed sample over the entire image during training. To evaluate this method effectiveness, we train a model using offset noise and conduct tests both with and without noise offsetting.

While we do not find significant differences using clipping, offset noise or both quantitatively (*cf.* Table 7), we have encountered an increase in details in some classes using clipping. However, the generated meshes generally contained more holes.

Category	Clip	Offset	1-NNA ↓		MMD ↓		COV ↑	
			CD	EMD	CD	EMD	CD	EMD
Airplane	✓		72.79 ± 1.11	69.67 ± 1.34	0.31 ± 0.01	<b>0.50</b> ± 0.01	<b>47.90</b> ± 1.02	<b>47.70</b> ± 1.19
		✓	<b>71.35</b> ± 0.96	71.62 ± 1.17	0.31 ± 0.01	0.51 ± 0.00	46.15 ± 0.98	45.43 ± 1.58
	✓	✓	72.98 ± 1.22	<b>69.43</b> ± 1.13	0.31 ± 0.01	0.51 ± 0.00	45.65 ± 1.35	46.32 ± 1.54
Bike	✓		64.41 ± 5.27	67.21 ± 6.58	<b>1.71</b> ± 0.06	<b>1.16</b> ± 0.06	45.88 ± 3.97	<b>57.35</b> ± 3.98
		✓	<b>62.94</b> ± 6.96	<b>66.62</b> ± 6.97	1.72 ± 0.11	1.19 ± 0.07	47.35 ± 5.79	54.71 ± 4.64
	✓	✓	64.12 ± 6.17	69.12 ± 5.46	1.76 ± 0.06	1.18 ± 0.06	<b>50.00</b> ± 7.72	54.71 ± 5.41
Car	✓		66.73 ± 0.77	63.17 ± 1.06	0.90 ± 0.01	0.65 ± 0.01	<b>37.75</b> ± 1.55	42.29 ± 1.27
		✓	<b>67.69</b> ± 0.76	62.29 ± 1.21	<b>0.89</b> ± 0.01	<b>0.65</b> ± 0.00	35.60 ± 1.48	<b>43.40</b> ± 2.11
	✓	✓	67.74 ± 1.17	<b>61.87</b> ± 1.36	0.90 ± 0.01	0.66 ± 0.01	34.09 ± 1.26	41.63 ± 0.84
Chair	✓		64.59 ± 0.37	<b>63.07</b> ± 0.68	<b>4.85</b> ± 0.09	<b>2.47</b> ± 0.03	<b>45.50</b> ± 0.69	<b>47.48</b> ± 0.84
		✓	<b>62.71</b> ± 0.43	63.72 ± 0.73	5.01 ± 0.04	2.51 ± 0.02	44.46 ± 0.75	46.56 ± 0.70
	✓	✓	63.66 ± 0.69	63.91 ± 0.78	4.99 ± 0.09	2.52 ± 0.03	42.90 ± 0.95	46.34 ± 0.82

Table 7. Comparison of clipping and offset noise during inference on ShapeNet classes airplane, bike, car and chair. Only the outer surface was sampled. Reference dataset was sampled from ShapeNet ground truth. MMD-CD is multiplied by  $\times 10^3$ , EMD by  $\times 10^2$ .